Water Research 239 (2023) 120022

Contents lists available at ScienceDirect

Water Research

journal homepage: www.elsevier.com/locate/watres

Magnetic anaerobic granular sludge for sequestration and immobilization of Pb

Rui Zhou [a], Han Li [a], Chengshuai Liu [b], Yizhang Liu [b], Jyh-Fu Lee [c], Yu-Jung Lin [c], Zhang Yan [a], Zhangyi Xu [a], Xiaoyun Yi [a], Chunhua Feng [a,*]

[a] *The Key Lab of Pollution Control and Ecosystem Restoration in Industry Clusters, Ministry of Education, School of Environment and Energy, South China University of Technology, Guangzhou 510006, PR China*
[b] *State Key Laboratory of Environmental Geochemistry, Institute of Geochemistry, Chinese Academy of Sciences, Guiyang 550081, PR China*
[c] *National Synchrotron Radiation Research Center, Hsinchu 30076, Taiwan, ROC*

ARTICLE INFO

Keywords:
Heavy metal stabilization
Iron-based remediation material
Anaerobic granular sludge
Magnetic adsorbent
Pb pollution
Field remediation

ABSTRACT

The development of magnetic adsorbents with high capacity to capture heavy metals has been the subject of intense research, but the process usually involves costive synthesis steps. Here, we propose a green approach to obtaining a magnetic biohybrid through in situ grown anaerobic granular sludge (AGS) with the help of magnetite, constituting a promising adsorbent for sequestration and immobilization of Pb in aqueous solutions and soils. The resultant magnetite-embedded AGS (M-AGS) was not only capable of promoting methane production but also conducive to Pb adsorption because of the large surface area and abundant function groups. The uptake of Pb on M-AGS followed the pseudo-second order, having a maximum adsorption capacity of 197.8 mg gDS^{-1} at pH 5.0, larger than 159.7, 170.3, and 178.1 mg gDS^{-1} in relation to AGS, F-AGS (ferrihydrite-mediated), and H-AGS (hematite-mediated), respectively. Mechanistic investigations showed that Pb binding to M-AGS proceeds via surface complexation, mineral precipitation, and lattice replacement, which promotes heavy metal capture and stabilization. This was evident from the increased proportion of structural Pb sequestrated from the aqueous solution and the enhanced percentage of the residual fraction of Pb extracted from the contaminated soils.

1. Introduction

Heavy metal contamination in aquatic environments and soils is a worldwide concern for ecosystems and human health, which has stimulated considerable interest in developing effective and environmentally friendly solutions for removing or separating heavy metals from polluted media (Barakat, 2011; Qin et al., 2021). Owing to its high efficiency, simple operation, good reproducibility, and flexible design, adsorption is considered an economical and effective strategy. To achieve high adsorption performance, plenty of functional materials with high surface area, abundant chemical groups, and low cost have been exploited as adsorbents in previous reports (Bhateria et al., 2019; Bilal et al., 2021; Dave et al., 2014). Among them, magnetic adsorbents stand out as promising materials for heavy metal uptake, thanks to the benefits of rapid separation and recovery by an external magnetic field (Feng et al., 2020). Increasing attention has been paid to using magnetite (Fe_3O_4) for sequestrating toxic metals because of its super magnetism, biocompatibility, and existence as natural minerals on Earth (Karami, 2013; Namdeo, 2018). Further studies have been conducted to increase the adsorption capacity of magnetite through functionalized modification on the surface. For example, the hydroxyl, amino, carboxyl, and carbonyl groups were introduced to aid in metal chelation (Li et al., 2022b; Mahdavian et al., 2010; Shi et al., 2015). Despite their advances, magnetite-organic composites might suffer from the problem of complexity in preparation, which involves extensive energy and chemical consumption (Al-Khateeb et al., 2022). This aroused our interest in synthesizing magnetite-based adsorbents in a green and sustainable fashion.

Inspired by the natural phenomenon in which the combination of Fe minerals and biological materials in environments results in a biohybrid composite with a high-degree affinity for heavy metals (Cui et al., 2022; Wang et al., 2014; Zhang and Wang, 2020), we intend to prepare magnetite-embedded anaerobic granular sludge (AGS), which emerges as a promising solution for heavy metal capture. Indeed, AGS was

---

* Corresponding author.
E-mail address: chfeng@scut.edu.cn (C. Feng).

https://doi.org/10.1016/j.watres.2023.120022
Received 25 November 2022; Received in revised form 3 April 2023; Accepted 29 April 2023

regarded as an excellent biosorbent material due to its superior adsorption efficiency, dense and firm microbial structure, high biomass concentration, good settling capacity, and the ability to withstand shock loading (Hawari and Mulligan, 2006; Nancharaiah and Kiran Kumar Reddy, 2018; Wang et al., 2018a). Moreover, the utilization of conductive magnetite for AGS formation and, accordingly, facilitating anaerobic digestion for wastewater treatment and harnessing methane has been documented recently (Baek et al., 2017; Cruz Viggi et al., 2014; Kim et al., 2022). Direct interspecies electron transfer (DIET), an essential pathway in promoting the anaerobic digestion process, represents a syntrophic metabolism among microorganisms, in which electrons are transferred from one microbial cell to another via electrically conductive pili, cytochromes, and conductive materials without the participation of reduced electron carriers (such as H_2 and other redox mediators) (Gahlot et al., 2020; Wang et al., 2021). It has been demonstrated that magnetite can accelerate DIET in AGS and thus promote solubilization, hydrolysis, acidogenesis, and/or methanogenesis processes, which in turn enriches diverse microorganisms with improved enzymatic activity (Luo et al., 2022; Wang et al., 2018b). The AGS is mostly composed of extracellular polymers and microbial cells that inherently contain a variety of functional groups favorable for metal attachment. In general, the AGS is a waste product that must be treated safely and disposed of. The comprehensive utilization of AGS as a resource conforms to sustainable development principles. The creation of magnetite-embedded AGS (M-AGS) is thus not only conducive to methane generation from wastewater, but it also represents a desirable alternative among other sludge disposal technologies, since it can potentially function as a promising magnetic adsorbent for heavy metals in contaminated aquatic environments and soils.

Taking lead (Pb, one of the most toxic and non-biodegradable heavy metals frequently detected in environments) as an example, our central aim is to demonstrate the efficacy of M-AGS for the sequestration and immobilization of Pb from water and soil. The M-AGS composite was prepared in an upflow anaerobic sludge blanket (UASB) reactor with the incorporation of magnetite during the methanogenic degradation of organic matter. The adsorption kinetics and isotherms of Pb on magnetic AGS were evaluated. For comparison, ferrihydrite and hematite were also used to promote AGS growth and anaerobic methane generation, and the resultant AGS materials for Pb adsorption and stabilization were investigated. Moreover, Pb-binding mechanisms were elucidated through Fourier transform infrared spectroscopy (FTIR), X-ray diffraction spectra (XRD), X-ray photoelectron spectroscopy (XPS), scanning electron microscopy (SEM), and X-ray absorption spectroscopy (XAS) techniques. The findings acquired have the potential to provide an economically viable strategy for reutilizing AGS as a heavy metal-stabilizing material, including the future operation of anaerobic wastewater treatment in a sustainable manner.

2. Materials and methods

2.1. Anaerobic cultivation of Fe oxide-embedded AGSs

Lab-scale UASB reactors (37 cm in height and 14 cm in diameter) with a working volume of 2 L were operated to cultivate AGSs. The reactors made of Plexiglas were placed in a thermostatic incubator at 30 °C under anaerobic conditions. The initial 500 mL of AGS (Liboyuan Co. Ltd, Shandong, China) was used as the seed sludge added to the four reactors: one reactor without the addition of Fe minerals as a control, and three reactors, respectively fed with 500 mg L^{-1} ferrihydrite, hematite, and magnetite. The initial AGS was produced from the anaerobic digestion of fresh waste leachate with an organic loading rate of 7 kg COD m^{-3} day^{-3} in a UASB reactor made of stainless steel (coated with an anticorrosive material) with an internal diameter of 2 m and a height of 8 m (working volume = 25 m^3). All the Fe oxides were lab-prepared according to the procedures described previously (Schwertmann et al., 1989). The XRD patterns in Fig. S1 show their typical crystalline structures and confirm successful synthesis. The synthetic wastewater was composed of 3000 mg L^{-1} (glucose that was the most extensively substrate for the AGS formation was chosen as the carbon source), 160 mg L^{-1} N (NH_4Cl), 80 mg L^{-1} P (KH_2PO_4), 960 mg L^{-1} yeast extract, 3000 mg L^{-1} $NaHCO_3$, 38 mg L^{-1} $CaCl_2$, 80 mg L^{-1} $MgSO_4$, and 1.0 mL L^{-1} trace element solution. The composition of the trace element solution was (mg L^{-1}): $CuCl_2$ 30, $ZnCl_2$ 50, $MnSO_4$ 1100, and $CoCl_2$ 600. After 15 days of inoculation, the AGSs were immediately washed three times using deionized water, avoiding the influence of the surface-soluble ions on the experiments. The AGSs were then frozen in the refrigerator (−18 °C) for 6 h and dried in the vacuum lyophilizer for 24 h prior to further use in the adsorption tests. The dried M-AGS maintained the granular morphology, as shown in Fig. S2. The aggregate gas samples were collected in a 1 L foil gas bag during the 15-day inoculation period. The biogas production was assessed twice a week by determining the gas volume in the gas bag with a 500 mL syringe. The methane content was measured using gas chromatography (GC, Shimadzu 2014C, Japan) equipped with a GDX 104 column and a thermal conductivity detector. The injector, oven, and detector temperatures were controlled at 150, 100, and 160 °C, respectively. Helium gas with a 99.999% purity was used as the carrier gas in the system. The wet AGS samples collected directly from the UASB reactors were used for genomic DNA extraction and microbial community analysis. For each sample, the integrity of the DNA was examined by electrophoresis on 1.0% agarose gels, and the PCR products were quantified. Paired-end sequencing was conducted using the high-throughput sequencing platform MiSeq (Illumina, USA). Sequences were clustered into operational taxonomic units (OTUs) with a 97% similarity level using the UPARSE method.

2.2. Batch experiments for Pb adsorption onto AGSs in an aqueous solution

The adsorption kinetics experiments were conducted in a 250 mL Erlenmeyer flask containing 100 mg (dry weight) of materials and 200 mL of Pb solution (120 mg L^{-1}). The initial pH value was set to 5.0 using 0.1 mol L^{-1} HNO_3 and 0.1 mol L^{-1} NaOH solutions. Samples were collected at specified time intervals and passed through a 0.22-μm polycarbonate filter. The filtered liquids were subjected to chemical analysis of the aqueous Pb concentration, which was determined using an atomic absorption spectrophotometer (AAS) (Optima 5300 DV, San Diego, USA). After reaching adsorption equilibrium, the remaining solids were dried in a vacuum lyophilizer for 24 h for subsequent characterizations. For the adsorption isotherm experiments, AGSs with a dry weight of 40 mg were added to the 80 mL solution with the initial Pb concentrations varying from 20 to 120 mg L^{-1}. The Erlenmeyer bottles were placed in a 30 °C thermostatic shaker at 150 rpm for 6 h to ensure equilibrium. The supernatant of each solution was filtered through a 0.22-μm polycarbonate filter and the residual Pb concentration in the solution was determined. The effect of the initial pH on the adsorption performance was investigated in the same reactor containing 40 mg AGS and 100 mg L^{-1} Pb in a pH range between 2.0 and 5.0 (Note that the pH value beyond 5.0 easily caused precipitation of $Pb(OH)_2$). The adsorbed and structural Pb concentrations were quantified based on procedures described previously (Frierdich et al., 2015). Briefly, Pb-containing AGSs measuring 200 mg was mixed with 10 mL of 0.4 mol L^{-1} HCl, and the mixture was placed in a centrifuge tube and reacted in a rotary oscillator for 0.5 h. The supernatant was centrifuged at 8000 rpm for 5 min, and the content of dissolved Pb was measured as the adsorbed Pb. The difference in the adsorbed Pb concentration and the total content of Pb in the AGSs was denoted as the structural one. All the above experiments were performed in triplicate, and average data values were reported.

For calculations, the removal efficiency of Pb was calculated as a percentage (%R) and as the quantity of adsorbed Pb (Q_e), according to Eqs. (1) and (2), expressed as follows:

$$\%R = \frac{(C_0 - C_t)}{C_0} \times 100\% \tag{1}$$

$$Q_e = \frac{(C_0 - C_t) \times V}{m} \tag{2}$$

where V (L) is the volume of adsorbate solution, m (g) refers to the mass of adsorbents, Q_e (mg g^{-1}) is the adsorbed amount, and C_0 and C_t represent aqueous Pb concentrations (mg L^{-1}) before and after adsorption at time t (min), respectively. To better investigate the adsorption kinetics, the time-dependent experimental data of Pb onto AGSs were analyzed according to the pseudo-first-order model (Eq. (3)), the pseudo-second-order model (Eq. (4)), and the intra-particle diffusion kinetic model (Eq. (5)).

$$\ln(Q_e - Q_t) = \ln Q_e - K_1 t \tag{3}$$

$$\frac{t}{Q_t} = \frac{1}{K_2 Q_e^2} + \frac{1}{Q_e} t \tag{4}$$

$$Q_t = K t^{1/2} + C \tag{5}$$

where Q_t (mg g^{-1}) refers to the adsorbed amount at time t, Q_e (mg g^{-1}) is the adsorbed amount at equilibrium, K_1 (min^{-1}) is the rate constant of pseudo-first-order kinetics model, K_2 (mg g^{-1} min $^{-1}$) stands for the equilibrium rate constant of the pseudo-second-order kinetics model, and K is the rate constant of intra-particle diffusion (mg g^{-1} $min^{-1/2)}$, calculated from the slope of the straight line of Qt versus $t^{1/2}$. C is the value of the intercept of stage i, giving an idea about the boundary layer thickness. To understand the adsorption equilibrium, the Langmuir model (Eq. (6)), Freundlich model (Eq. (7)), and Temkin isotherm model (Eq. (8)) were used for data fitting.

$$Q_e = Q_m \frac{K_L C_e}{1 + K_L C_e} \tag{6}$$

$$Q_e = K_f C_e^{1/n} \tag{7}$$

$$Q_e = \frac{RT}{B} \ln A + \frac{RT}{B} \ln C_e \tag{8}$$

where C_e (mg L^{-1}) is the equilibrium concentration of Pb, Q_e (mg g^{-1}) refers to the adsorption capacity, Q_m (mg g^{-1}) represents the theoretical maximum sorption capacity, K_L (L mg^{-1}) is the Langmuir constant related to adsorption energy, K_f is the binding energy constant reflecting affinity of adsorbents to Pb, and n is the Freundlich constant, A (L g^{-1}) and B (J mol^{-1}) are Temkin constants, R is the ideal gas constant (8.314 J mol^{-1} K^{-1}), and T (K) is the absolute temperature.

2.3. Physicochemical characterizations of AGSs before and after Pb adsorption

The physical morphology of the samples was examined using a scanning electron microscope (SEM, Merlin, Zeiss Co., Berlin, Germany). The Brunauer-Emmett-Teller (BET, Micromeritics ASAP 2460, USA) method was employed to analyze the BET surface area, total volume of pores, and average diameter of pores in the AGSs. The dried materials were also powdered using a mortar-pestle and characterized with various instrumental techniques, as elaborated below. The surface charge of the samples was recorded by measuring the zeta potential using a potential analyzer (NanoBrook 90 Plus Zeta, Brookhaven Instrument Co., Ltd., USA). XRD patterns were collected on an X-ray diffractometer (Bruker D8 Advance diffractometer, Almelo, The Netherlands) at the 2θ scanning range of 5–90° with Cu Kα radiation (40 kV, 40 mA). Fourier transform infrared spectroscopy (FTIR) spectra were obtained via the FTIR analyzer (Bruker VERTEX 70, Waltham, MA, USA) over the spectral range from 4000 to 400 cm^{-1}. X-ray photoelectron spectroscopy (XPS, ESCALAB250Xi, Thermo Fisher Scientific, Waltham, MA, USA) was used to study elemental composition on the surfaces of composites. The X-ray absorption spectroscopy (XAS) test was completed at the Taiwan Synchrotron Radiation Facility. All samples were measured by fluorescence modes, and a Lyter-type fluorescence ionization chamber was used as a detector. The X-ray absorption near edge structure (XANES) and Extended X-ray absorption fine structure (EXAFS) spectra of Fe K-edge and Pb L-edge were collected from the samples. The obtained XAS data was processed in Athena (version 0.9.26) for background, pre-edge line, and post-edge line calibrations. Then, Fourier transformed fitting was carried out in Artemis (version 0.9.26) (Ravel et al., 2005). The magnetic properties of samples were measured using a vibrating sample magnetometer (VSM) (Lake Shore 7404, Columbus, OH, USA) with a magnetic field strength of 20 kOe at room temperature (25 °C). The electrical conductivity data were acquired on an ST2722-SD powder resistivity testing instrument (Suzhou Lattice Electronics Co., Ltd, Suzhou, China) with an ST2255 test module. The Fe mineral powders were pressurized to different heights, and then the resistivity of the cylindrical sample was measured using the four-point probe method. The Mössbauer spectroscopy was employed to characterize the occupied states of Fe in M-AGS. It was performed on a spectrometer (WSS-10, WissEL GmbH, Germany) equipped with a closed-loop cryostat (SHI-850, Janis Research Co., USA). The sample was collected on a 0.22-μm nitrocellulose filter membrane and sealed between two pieces of Kapton tape with copper rings after drying in an anaerobic box. The Mössbauer spectra of M-AGS were taken at room temperature in the range of −10 to +10 mm s^{-1}. The experimental data was calibrated with α-Fe^0 foil and fitted using MossWinn official software (version 4.0 Pre).

2.4. Tests on the utilization of AGSs for immobilization of Pb in contaminated soils

More efforts were made to investigate the efficacy of M-AGS for the sequestration and immobilization of Pb from the contaminated soil. The soil samples used in this experiment were collected from an electroplating plant (N25°12′34″, E109°24′3″, Liuzhou, Guangxi, China). All samples were placed in polyethylene bags and brought to the laboratory, and then stored in a refrigerator at 4 °C. After removing the stones and coarse debris, the air-dried soils were grounded in an 80-mesh nylon sieve for further chemical analysis and experiments. The stabilizing experiments were set up in a 100 mL centrifuge tube, in which the soil (50 g) sample and AGSs existing at a ratio of 5% (w/w dry weight of AGS to soil) were added. Water was amended to maintain the soil moisture at a 1:1 (v/v) water–soil ratio during the whole process. All test samples were placed in the shaker at 25 °C for 28 days. All treatments were replicated three times. Samples were taken every week to analyze the distribution of Pb fractions and the leaching toxicity of soil samples.

For analysis, the soil was digested with an HCl-HNO_3-$HClO_4$-HF mixed solution (10:9:3:1, v/v), and the total concentrations of heavy metals in the soil were quantified using AAS. Blank controls and standard reference materials (GBW07390, GSS-34) were included in each batch of digestion. A Chinese leaching procedure—HJ-299 (Ministry of Ecology and Environment of the People's Republic of China, 2007)—was conducted to determine the leached metalloid concentrations from soil samples, and the sulfuric acid and nitric acid mixture liquid (v/v ratio of 2:1) was used as the leaching solution (diluted in 1 L of water with a pH value of 3.2). Table S1 lists the total and acid-extracted concentrations of the main heavy metals in the contaminated soils. It is evident that Pb was the predominant pollutant, with a total content of 1744.4 mg kg^{-1} and a leaching content of 0.68 mg L^{-1}, exceeding the Standard of Soil Environmental Quality in China (GB 36600-2018, Type I site control value) and the standard for groundwater quality (GB/T 14848-2017, Type IV limit value), respectively. The sequential extraction approach of the European Community Bureau of Reference (BCR) was applied to distinguish exchangeable (F1), reducible (F2), oxidizable (F3), and residual (F4) fractions of Pb in soils. The sequential extraction procedure was conducted step-by-step, as depicted in Table S2.

3. Results and discussion

3.1. Characterizations of Fe oxide-embedded AGSs regarding methane generation capacity, microbial community, and physicochemical properties

Three different Fe minerals, including ferrihydrite, hematite, and magnetite, were selected as the substrate to support the growth of AGSs for methane generation, and the resultant solid was named F-AGS, H-AGS, and M-AGS, respectively. It is notable from Fig. 1a that the incorporation of Fe oxides in AGSs had a positive effect on methane production from the anaerobic digestion of organic matter, in accordance with previous results (Tang et al., 2021; Wang et al., 2020; Ye et al., 2018). This finding might be explained by the facts that i) the Fe oxides introduced into AGS function as conducive materials, which facilitate cell-to-cell connection, increase the electrical capacitance of extracellular polymeric substance (EPS), and thereby promote DIET from acidogens to methanogens (Li et al., 2022a; Wang et al., 2018b); ii) the Fe oxides can establish intercellular connections between microorganisms and organic matter through adsorption, netting, or bridging, then forming a magnetite-AGS co-substrate, which can facilitate interspecies material exchange and energy transfer between microorganisms (Cui et al., 2022); and iii) the Fe oxides are able to act as counter ions binding to the negative-charged EPS in AGSs, and thus enhancing the metabolic activity of microorganisms for anaerobic digestion (Zhang et al., 2022). Among all the investigated cases, the M-AGS exhibited the best capacity for methane generation, which should be attributed to its higher electrical conductivity (0.004, 3.600, and 113.900 μS cm^{-1} for ferrihydrite, hematite, and magnetite, respectively). The differentiation in methane generation performance was manifested by the distinct change in the microbial community between the four reactors, as revealed in Fig. 1b. In particular, a sequence assigned to *Trichococcus* (belonging to *Firmicutes*) was apparently enriched in H-AGS and M-AGS but not in F-AGS. More importantly, the M-AGS revealed a profound enhancement in the abundance of *Trichococcus*. Groups of *Trichococcus* have been reported as fermentative bacteria that can use various organics, including acetate, formate, ethanol, glucose, and aromatic compounds, for anaerobic methane generation (Ma et al., 2021). A previous study (Tang et al., 2021) utilizing methanogenic sludge for the treatment of dairy wastes also demonstrated that Fe(III) oxides (hematite and magnetite) could specially cultivate *Trichococcus* species, which is considered an electroactive Fe-reducing bacterium accelerating DIET with *Methanothrix* species in syntrophic degradation of complex organic compounds. However, the ability of *Trichococcus* to achieve extracellular electron transport has not been reported and deserves future exploration (which is beyond the scope of the current study).

Chemical analysis of the Fe uptake rate and the proportion of Fe in the resultant AGSs was performed. Fig. S3a shows that the Fe uptake rate was in the order of M-AGS > H-AGS > F-AGS > AGS. The M-AGS achieved a maximum Fe load of 124.0 mg gDS^{-1} after 15 days, exceeding the values of 33.6, 92.1, and 94.9 mg gDS^{-1} in relation to AGS, F-AGS, and H-AGS, respectively (Fig. S3b). This indicates that magnetite was more inclined to be incorporated into AGS, possibly due to its competitive ability to substitute metallic counter ions (e.g., Ca, Mg, and Al) (Ajao et al., 2020; Sudmalis et al., 2020). It is further shown that more than 90% of Fe was bound with the microbial cells, suggesting that the majority of Fe minerals were loaded into the inner part rather than the outer part (e.g., EPS) of AGS. These findings support the view of the engagement of Fe minerals (particularly magnetite) in promoting cell-to-cell electron transfer (Cruz Viggi et al., 2014; Kang et al., 2021; Wang et al., 2020). Fig. S4 presents the zeta potentials of the AGSs. The values associated with the Fe mineral-involved AGSs shifted positively compared to that of the unmodified AGS, suggesting the enhanced electrostatic interaction between Fe oxides and the AGS. Because of stronger binding, the M-AGS processed a higher zeta potential of 2.33, which indicates negatively charged surfaces available for cationic heavy metal adsorption at pH beyond this value. Comparisons of the magnetic properties between different samples are depicted in Fig. 1c, which depicts the magnetization hysteresis curves of four materials with the

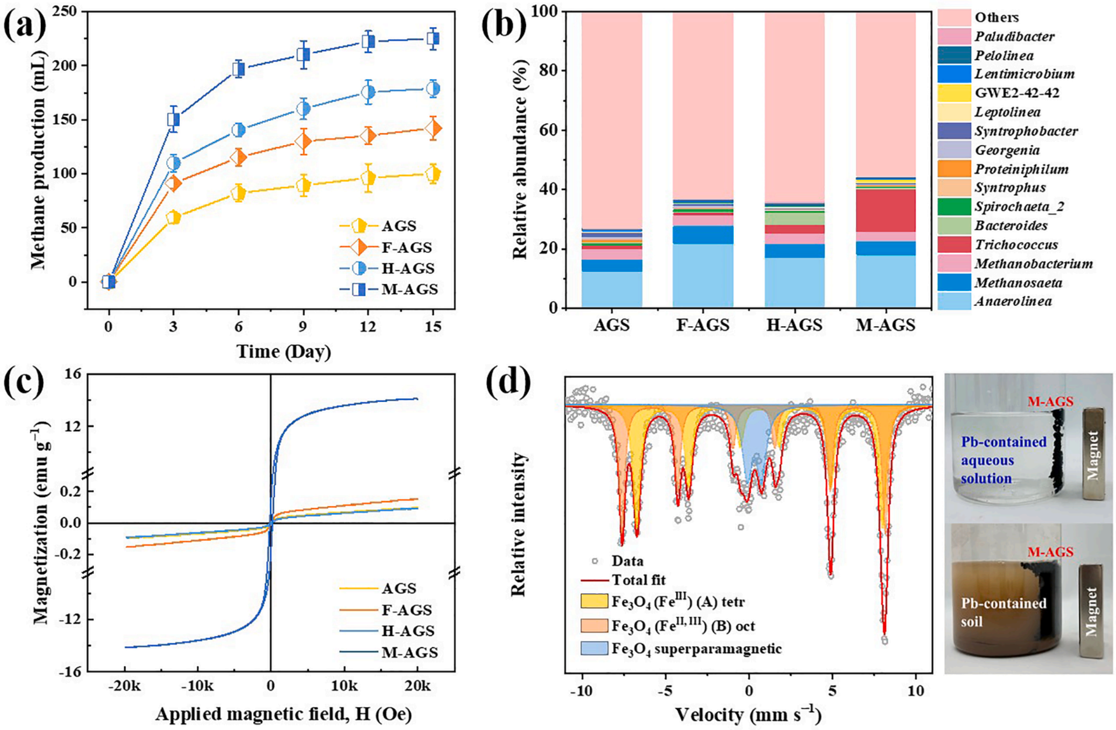

Fig. 1. (a) Methane production in UASB reactors, (b) microbial community at the genus level, (c) magnetization curves in relation to different AGSs, and (d) Mössbauer spectra of M-AGS. The Mössbauer spectra were calibrated against a 7 μm α-Fe^0 foil and fit using MossWinn software.

field sweeping from −20,000 to 20,000 Oe. It was found that the M-AGS exhibited an excellent magnetic feature with a saturation magnetization of 13.3 emu g^{-1}. The reversible hysteresis curve with almost zero retentivity and coercivity confirmed the superparamagnetic nature of M-AGS. Fig. 1d shows the room-temperature Mössbauer spectra of M-AGS, and the hyperfine parameters for data fitting are given in Table S3. In general, the spectra of M-AGS contained a Zeeman sextet with broadened resonance lines (characteristic of Fe_3O_4) and a quadrupole doublet (characteristic of the superparamagnetic state of Fe^{2+} and Fe^{3+}) (Zheltova et al., 2020). The asymmetric shape and the broadening of the spectral lines are likely induced by the presence of regions of disorder in the structure. The Mössbauer spectra could be deconvoluted into two sub-sextets (one corresponding to Fe^{III} in the tetrahedral [A] site [37.90%] of magnetite and the other relevant to Fe^{II} and Fe^{III} in the octahedral [B] site [45.48%] of magnetite) and one doublet associated with superparamagnetic phase (16.62%). The magnitude of the hyperfine magnetic field for the M-AGS sample was equal to 49.0 ± 0.1 T, which validates the magnetic properties of M-AGS (Si et al., 2004; Daou et al., 2006). This feature made it a promising magnetic adsorption material beneficial for separating and recovering targeted contaminants in either the aqueous phase or soil (outer picture of Fig. 1d).

The specific surface area was evaluated using the N_2 adsorption–desorption isotherms of the BET tests. Table S4 shows that the M-AGS was featured with a larger surface area, a higher mesoporous pore volume, and a smaller particle size than its counterparts, indicating its advantages for metal attachment. For example, the surface area of M-AGS, H-AGS, F-AGS, and AGS was 10.96, 6.89, 1.11, and 0.25 m^2 g^{-1}, respectively. The SEM observations accorded well with the variations in the specific surface area. As illustrated in Fig. 2, the control AGS sample was densely packed, and the introduction of Fe minerals induced the granule to become loose. A more distinct difference was disclosed in the interior of AGS. In comparison to the stacked structure of AGS, the Fe mineral-embedded AGSs (particularly M-AGS) were enriched with filamentous bacteria and had porous structures. This morphology should be favorable to the affinity of heavy metals.

3.2. M-AGS for sequestration and stabilization of Pb in aqueous solution

The kinetics of Pb adsorption on AGSs were performed and compared between different samples by contacting 120 mg L^{-1} Pb at pH 5.0 (it should be noted from Fig. S5 that the maximum adsorption amount was attained at this pH value for all the cases). The dosage of M-AGS was set at 0.5 g L^{-1}, where the capacity of Pb adsorption reached a maximum value (Fig. S6). The dry sludge was used for the adsorption tests, as the maximum adsorption capacity of dry sludge was about 5–18% higher than that of wet sludge (Fig. S7). This might be because the dry sludge had a larger surface area and provided more surface-active sites for adsorption (Wei et al., 2008).

The time-course aqueous Pb concentration for all cases was recorded in Fig. 3a, which clearly indicated the difference in the percentage of Pb removal between different treatments. The M-AGS enabled a removal efficiency of 84.6% after a 1440-min operation, which was larger than the removal efficiency of 76.2%, 72.9%, and 68.3% in relation to H-AGS, F-AGS, and AGS, respectively. Fig. 3b shows that the adsorption capacity for all cases enhanced rapidly during the first 100 min, followed by a gradual increase from 100 to 400 min and reaching equilibrium after 400 min. This adsorption behavior has been frequently reported with respect to a variety of adsorbents for Pb uptake (Basu et al., 2017; Ling et al., 2017; Liu et al., 2020; Naushad et al., 2021). The fast adsorption during the initial stage was due to the presence of abundant adsorption sites on the adsorbent. The initial metal concentration gradient provided an important driving force to overcome the mass transfer resistance between the aqueous and adsorbent, which is also responsible for this phenomenon. The M-AGS outperformed the other materials in terms of higher equilibrium adsorption capacity (197.8 mg gDS^{-1}) than AGS (159.7 mg gDS^{-1}), F-AGS (170.3 mg gDS^{-1}), and H-AGS (178.1 mg gDS^{-1}). Moreover, the adsorption of Pb on AGSs was fitted with the pseudo-first-order, pseudo-second-order, and intra-particle models (Fig. S8) and the kinetic parameters and correlation coefficients are listed in Table S5. It is apparent that the pseudo-second-order kinetic model was more appropriate for predicating the adsorption of Pb because of the higher correlation coefficient. The calculated equilibrium adsorption capacities based on the pseudo-second-order model agreed well with the experimental values. This suggests that the rate-limiting step in this adsorption process could be chemisorption (Esrafili et al., 2021; Shi et al., 2015). The adsorption isotherms were obtained by varying the initial Pb concentrations from 20 to 120 mg L^{-1} at pH 5.0. Fig. 3c shows that the adsorption capacities of Pb on AGSs increased with increasing Pb content and reached equilibrium at a particular value due to the lack of available sites for adsorbing metal ions. The adsorption data were fitted by the Langmuir, Freundlich, and Temkin isotherm models (Fig. S9), and the fitting parameters are given in Table S6. The data were more reasonably fitted with the Langmuir model, indicating that the monolayer adsorption on AGSs dominates the process (Esrafili et al., 2021; Liu et al., 2020). According to the fitting results, the M-AGS exhibited superior capability for Pb adsorption, evident from its distinctly higher maximum adsorption capacity (200.0 mg gDS^{-1}) than the others (AGS: 171.9 mg gDS^{-1}, F-AGS:174.6 mg gDS^{-1}, and H-AGS:180.3 mg gDS^{-1}).

It is generally accepted that the adsorption of heavy metals by weak bonding (e.g., ion exchange and electrostatic attraction) is vulnerable to potential risk of their re-release upon changes in environmental factors, such as pH value and coexisting ions (Caporale et al., 2015) and that

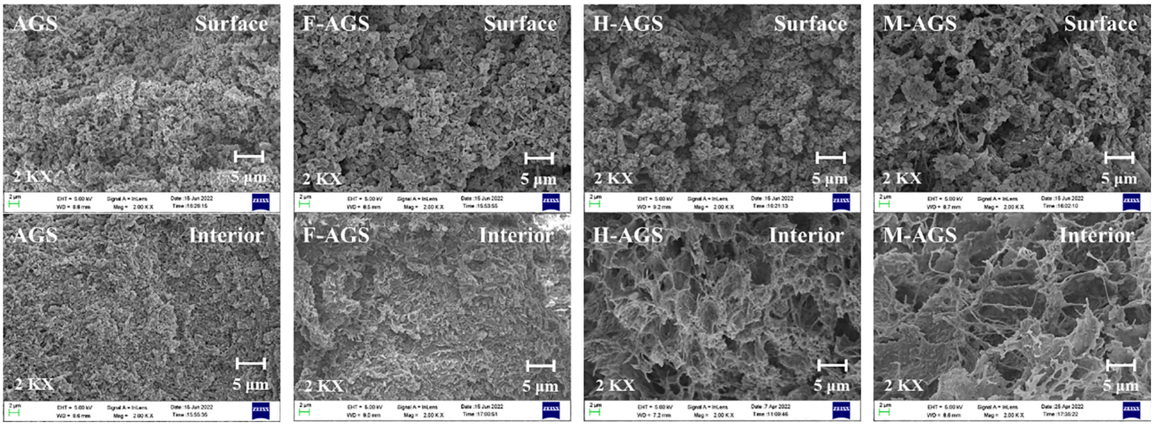

Fig. 2. SEM images of the surface and interior of different AGSs.

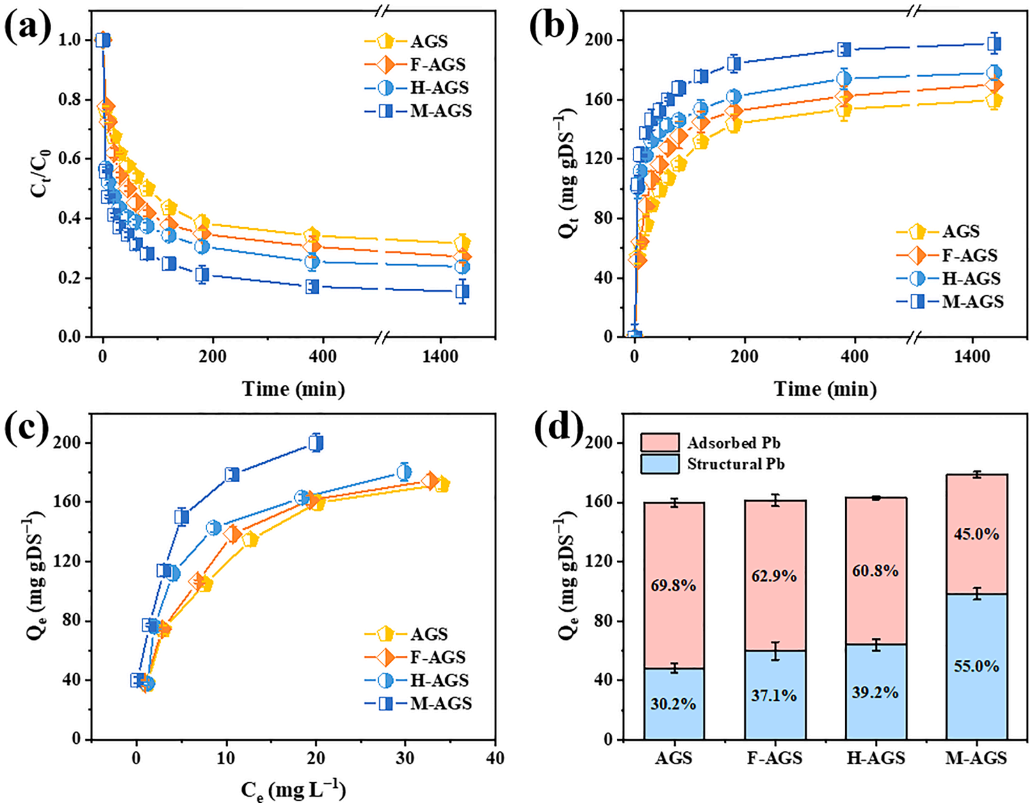

Fig. 3. Effects of the contact time on (a) the percentage of Pb removed from the aqueous phase and (b) the amount of Pb adsorbed on different AGSs under the experimental conditions: initial Pb concentration = 120 mg L^{-1}, volume = 200 mL, dosage of adsorbents = 100 mg, and pH = 5.0. (c) Effect of the initial Pb concentration on the amount of adsorbed Pb and (d) distribution of adsorbed and structural Pb in different AGSs under the experimental conditions: contact time = 360 min, volume = 80 mL, dosage of adsorbents = 40 mg, pH = 5.0, initial Pb concentration = 20-120 mg L^{-1} for (c & d), and initial Pb concentration = 100 mg L^{-1} for (d). Error bars represent the standard errors of triplicate tests, which were normally within ±5%.

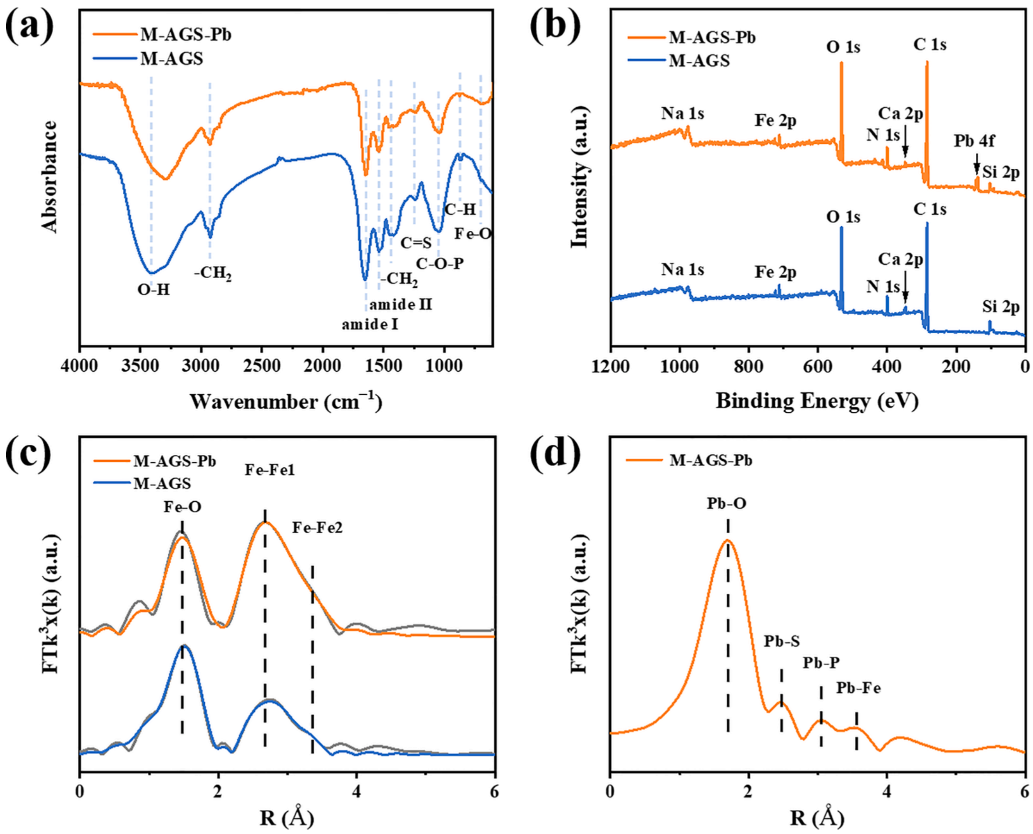

Fig. 4. (a) FTIR spectra, (b) XPS survey spectra, and (c) Fourier transforms of Fe K-edge EXAFS for M-AGS before and after Pb adsorption (both the measured data [gray lines] and the corresponding combination fits [colored lines] are shown). (d) Fourier transforms of Pb L-edge EXAFS for M-AGS after Pb adsorption.

strong bonding via adsorption mineralization, coordination complexation, and structural embedding allows the adsorbed heavy metals to be less influenced by the environment and have lower mobility (Ma et al., 2022). Therefore, an analysis of the distribution of adsorbed and structural Pb in the solid phases of the different samples was performed according to previous procedures (Friedrich et al., 2015). An interesting observation from Fig. 3d is that the involvement of Fe minerals inside AGSs appreciably improved the proportion of Pb incorporated into the structure of the sorbents. In particular, the M-AGS enabled more amounts of Pb firmly attached, likely because of the formation of insoluble precipitates and the incorporation of Pb inside the Fe oxide lattice, which are more stable in the environment and difficult to extract by weak acids. This point will be discussed in later sections.

It should be noted that the absence of AGSs contributed to a small proportion of Pb removal. Fig. S10a shows that limited amounts of Pb were removed from the aqueous phase by pure minerals (e.g., 8.1% for ferrihydrite, 13.5% for hematite, and 17.6% for magnetite after 1400 min of operation). Fig. S10b and S10c indicate that the maximum adsorption capacities of ferrihydrite, hematite, and magnetite for Pb uptake were 19.1, 31.5, and 36.3 mg gDS^{-1} at pH 5.0, respectively, which were much lower than the values obtained with the corresponding materials in the presence of AGS. Moreover, the majority of adsorbed Pb on the minerals was in the loosely attached form, as illustrated in Fig. S10d. These findings confirm the importance of the combined effects of AGSs and Fe minerals on the capture of Pb.

3.3. Mechanisms of Pb adsorption on M-AGS and explanations of the enhanced adsorption capacity and strong bonding

The adsorption mechanisms were elucidated by conducting a series of physiochemical characterizations to reveal the differences in the relevant signals between the AGSs before and after Pb uptake. Fig. 4a shows the FTIR spectra of M-AGSs in the presence and absence of Pb. The broad and intense band located at 3373 cm^{-1} (O—H stretching vibration) (Li et al., 2017) shifted to 3316 cm^{-1} after the adsorption of Pb. The absorption peaks centered at 1647 and 1530 cm^{-1} represent amide I (C═O stretching vibration) and amide II (-CN and -NH bending vibration), respectively, which are closely related to the extracellular protein in M-AGS (Niu et al., 2016). The relatively decreased peak intensities reflect the possible interaction between the extracellular protein and Pb (Pagliaccia et al., 2022). The peak at 1225 cm^{-1} assigned to C═S stretching vibration was also observable, which decreases substantially in intensity after Pb adsorption, indicating that the sulfur-containing groups in M-AGS actively interacted with Pb (Li et al., 2015). Additionally, the Pb engagement provoked a phosphate group-relevant peak shifting from 1063 to 1035 cm^{-1} and attenuation in its intensity. Note that a new peak attributed to lattice vibration of Fe-O appeared at 705 cm^{-1} after Pb adsorption, likely suggesting the formation of an inner-sphere surface complex (Fe-O-Pb) between Fe hydroxyl groups and Pb (Yang et al., 2009). Based on the FTIR analysis, it can be deduced that surface complexation between Pb and the functional groups available in M-AGS should be a plausible mechanism accounting for the high adsorption capacity. This is considered to be the consequence of the firming interaction between the Lewis soft acid (Pb) and soft base (ligands such as hydroxyl, carboxyl, thiol, phosphoryl, and amide groups) (Esrafili et al., 2021; Yang et al., 2019). The FTIR spectra of other samples (Fig. S11) also suggested the involvement of multiple functional groups for Pb complexation, but the intensities of most peaks were lower than those associated with M-AGS, indicative of lower adsorption capacity. These observations agree with the pseudo-second-order adsorption kinetics that suggest a chemisorption process. The XPS analysis also provided information on the adsorption and chelation of Pb with the abundant surface groups in M-AGS. Successful Pb sequestration was evident from the appearance of its signal in the XPS survey spectrum (Fig. 4b). As illustrated in Fig. S12, the deconvolution of C1s, N1s, O1s, and P2p XPS spectra indicated that the uptake of Pb resulted in changes in the relevant contents of C═O, O—C═O, O—H, -NH—C═O, $-NH_2$, P═O, and P—O bonds and their binding energies, showing their functions as Lewis bases to complex with Pb (Esrafili et al., 2021; Wang et al., 2015).

The XAS studies were performed to gain information on the Fe and Pb coordination environments in M-AGS with and without Pb; this helps to understand the possible incorporation of Pb deeply into the inner structure of Fe(III) (oxyhydr) oxides. The Fe K-edge signals and the corresponding EXAFS fits are provided in Fig. 4c; the obtained parameters are listed in Table 1. The first two radial structure function (RSF) peaks of each spectrum are fitted with one Fe—O shell and two subshells of Fe atoms, with an interatomic distance of ~1.98, ~3.02, and ~3.47 Å, respectively. There were apparent decreases in the interatomic distance of the Fe—O shell (from 1.98 to 1.96 Å) and the first Fe—Fe shell (from 3.02 to 2.99 Å). This agrees well with the observation that the contraction in the local Fe environment possibly occurred in order to accommodate the larger ions (e.g., Cd, Pb, and Zn) in the structure (Kaur et al., 2009). Moreover, the coordination number (CN) of the Fe—Fe shells significantly increased as a result of Pb incorporation. For example, the CN of the first and second Fe-Fe shells rose from 3.5 ± 0.3 to 4.9 ± 0.5 and 1.7 ± 0.2 to 5.2 ± 0.6, respectively. This suggests that the bridge of Pb with the scattered FeO_6 octahedra prompted a transformation from a metastable form to a relatively stable one (Chen et al., 2020).

Further analysis of the Fourier transfer spectrum of Pb L-edge EXAFS is revealed in Fig. 4d, which is characterized by an oscillation dominated by backscattering from first-shell oxygen atoms around the central Pb atom. In addition to the Pb—O contribution at 1.72 Å (Chisholm-Brause et al., 1990), the RSF contained Pb—S bond at 2.49 Å (Sharma et al., 2004), Pb–P bond at 3.03 Å (Qu et al., 2022), and Pb–Fe bond at 3.55 Å (Xu et al., 2006), again supporting its close interaction with M-AGS. Overall, the interpretation of XAS data was complicated by the adsorbed Pb either on the surfaces or within the defects of the bulk areas of magnetite and the uncertainties in the shell fitting due to the data quality, and some Pb—Fe distances and shifts may not even be detected in the XAS measurements. The possible structural incorporation of Pb, however, was consistent with changes based on the acid extraction experimental results since the sole surface adsorption of metals was unable to impose impacts on the structure of the adsorbents (Lu et al., 2020).

The XRD characteristics of all samples (Fig. 5a) show the variations in the crystallinity and phase in the AGSs before and after Pb adsorption. For all the Fe mineral-embedded AGSs, no typical crystalline peaks attributed to the planes of hematite and magnetite were displayed, indicating that the initial Fe oxide particles entered the inner parts of the AGS or suffered from phase transformation to some extent. In addition to the weak diffraction peaks corresponding to the poorly crystalline SiO_2 (JCPDS: 49-0629), the peaks assigned to $CaSi_2O_5$ (JCPDS: 51-0092) appeared and were more prominent in M-AGS. This is because magnetite promoted the proliferation of AGS (Ren et al., 2018), which, in turn,

Table 1
Details of Fe K-edge EXAFS fitting parameters of M-AGS before and after Pb adsorption.

	Shell	CN	R (Å)	σ^2	ΔE_0	R factor
M-AGS	Fe—O	5.4 ± 0.1	1.98 ±0.01	0.0097	−2.6 ± 0.7	0.0024
	Fe—Fe1	3.5 ± 0.3	3.02 ±0.01	0.0147		
	Fe—Fe2	1.7 ± 0.2	3.47 ±0.01	0.0066		
M-AGS-Pb	Fe—O	6.0 ± 0.4	1.96 ±0.01	0.0095	−1.4 ± 1.5	0.0074
	Fe—Fe1	4.9 ± 0.5	2.99 ±0.01	0.0070		
	Fe—Fe2	5.2 ± 0.6	3.50 ±0.02	0.0051		

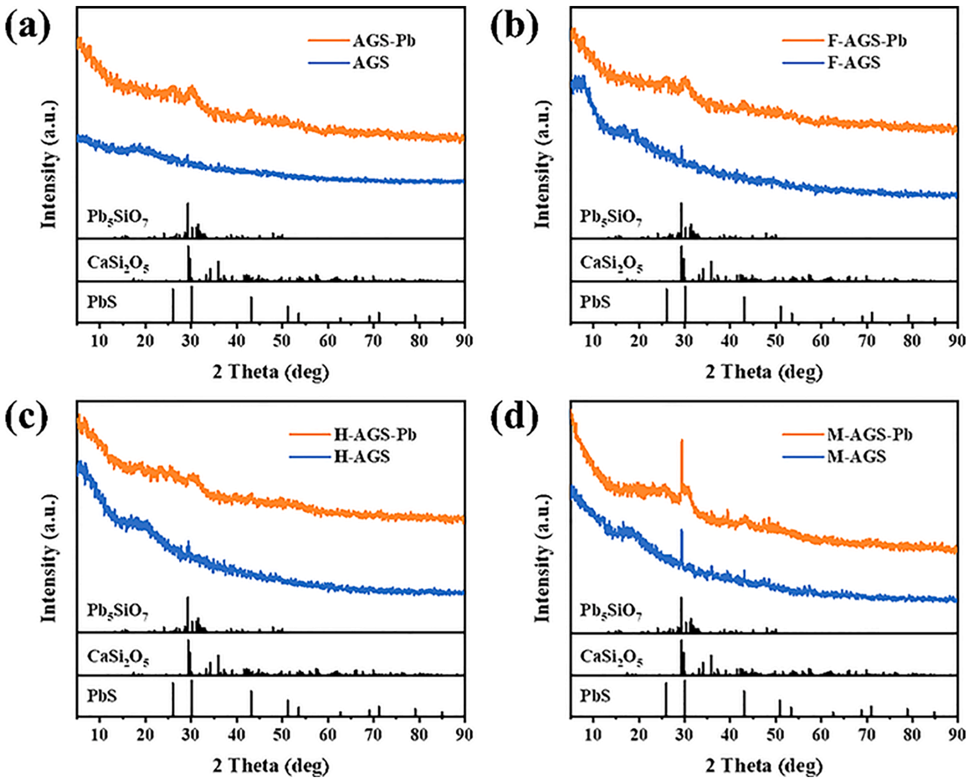

Fig. 5. XRD patterns of (a) AGS, (b) F-AGS, (c) H-AGS, and (d) M-AGS before and after Pb adsorption.

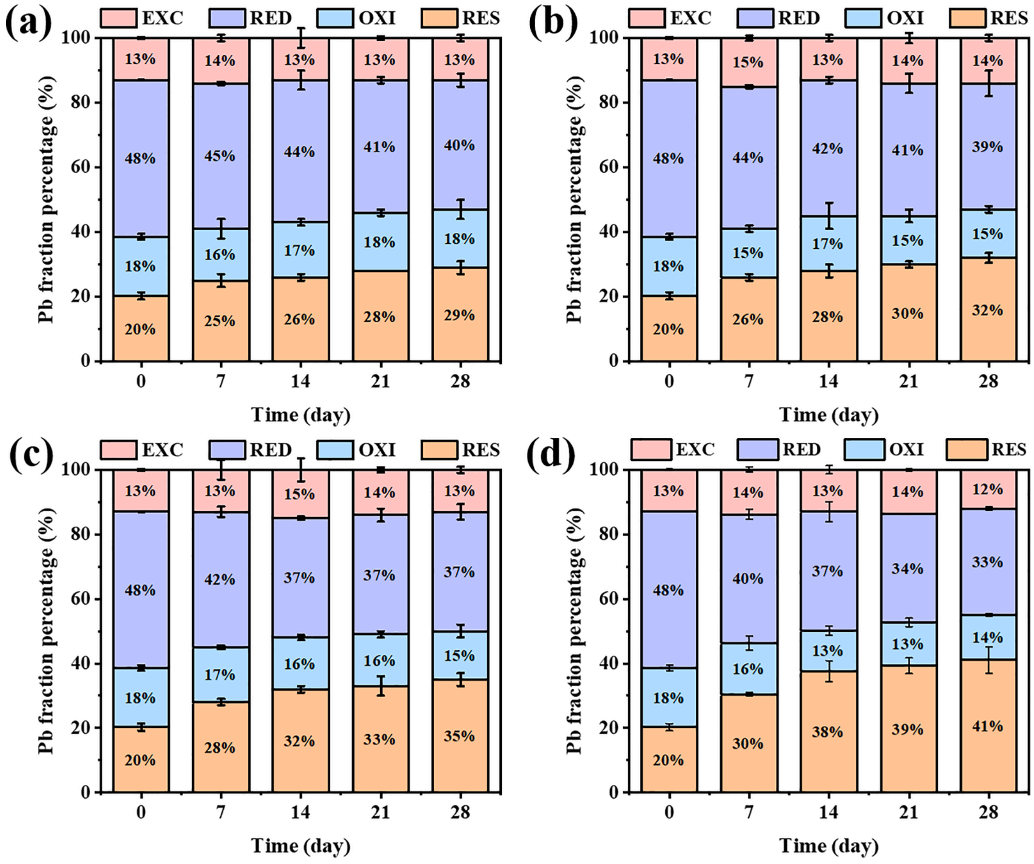

Fig. 6. Variations in Pb fractions in the contaminated soil as a result of treatment with (a) AGS, (b) F-AGS, (c) H-AGS, and (d) M-AGS. EXC: acid exchangeable fraction; RED: reducible fraction; OXI: oxidizable fraction; and RES: residue fraction. Error bars represent the standard errors of triplicate tests, which were normally within ±5%. In some cases, there appeared to be a 10% error in the data for Pb immobilization in the real contaminated soil.

yielded more amounts of Ca extracted from the aqueous culture. After Pb sequestration, new peaks relevant to Pb_5SiO_7 (JCPDS: 35-0274) and PbS (JCPDS: 99-0053) were observed, indicating the formation of Pb-containing crystals via the mechanism of precipitation. These compounds were also remarkably manifested in M-AGS-Pb. The formation of PbS is attributable to the strong affinity of Pb with the thiol groups, consistent with the aforementioned results (Ji et al., 2019). The generation of Pb_5SiO_7 is likely induced by lattice replacement (free Pb replaced Ca in the lattice of M-AGS) (Ma et al., 2022), followed by the hydrolysis $PbSi_2O_5$ particles to form Pb_5SiO_7 precipitates with low solubility. A similar phenomenon was also revealed in the survey XPS (Fig. 4b), in which the Ca-corresponding signal was completely diminished along with the appearance of Pb-relevant signals in M-AGS-Pb. The observation of these insoluble Pb precipitates also evidences the elevated level of structural Pb content in M-AGS, and it can be inferred that M-AGS has the potential to promote the stabilization of Pb.

3.4. Tests on M-AGS for immobilization of Pb in the contaminated soil

The capability to induce the structural incorporation of Pb makes M-AGS a potentially passivating material that immobilizes Pb available in the soil phase. To verify this, further experiments were conducted with real Pb-polluted soils using the AGSs as the stabilizing materials. Fig. 6 shows the relative abundance of Pb species in the soil samples before and after solidification by AGSs. The data were recorded by sequential extraction using the BCR, which included four fractions (Rauret et al., 1999). EXC refers to an acid-soluble exchangeable fraction; RED is a reducible fraction attached to the Fe—Mn oxides; OXI stands for an oxidizable fraction captured by organic matter and sulfides; and RES is the remaining residue in the mineral matrix. Generally, the EXC and RED fractions are considered to be more mobile and inclined to be released from the soil upon environmental changes, thus representing great risks to the environment (Salam et al., 2019). It should be noted that the proportion of EXC in all tested samples varied in a quite narrow range. This can be understood based on the fact that the use of acetic acid solution for extraction led to a pH below 3.0, at which the adsorption of AGSs to Pb declined vulnerably, thus masking the contribution of AGSs to the decrease in the acid-soluble fraction (Li et al., 2023). Comparisons of the distribution of Pb species after the exertion of different AGSs show that the unmodified AGS had limited capability to promote the immobilization of Pb. By contrast, the Fe oxide-involved AGSs apparently affected the proportion of Pb fractions, as the increasing operation time resulted in a gradual decrease in the percentage of RED and an increase in the percentage of RES. A more pronounced effect was achieved for M-AGS. For example, the 28-day duration prompted the residual fraction of Pb to rise to 41%, significantly higher than the 20% increase in the pristine soil. The reducible faction substantially decreased from 48% to 33% within the same period.

The leaching procedure tests were performed with the diluted acid (nitric acid and sulfuric acid) having a pH value of 3.2, which was added to the soil to extract Pb. The leached Pb concentration not only suggests the passivation efficiency of the material to the heavy metal but also acts as a benchmark that can be compared with the concentration limits in the groundwater quality standards. Fig. S13a shows that the 14-day operation reduced the Pb concentration in the leaching extract by 83.4% (from 0.68 to 0.11 mg L^{-1}) when the dry weight ratio of AGS to soil was 5%. Further increasing the duration to 28 days caused the leached Pb content to approach 0.05 mg L^{-1}, which is far below the limit value (0.10 mg L^{-1}) regulated for the groundwater quality of China (General administration of quality supervision inspection and quarantine of the People's Republic of China, 2017). Fig. S13b shows that the ratio of 3% might be insufficient in passivating Pb, as 0.12 mg L^{-1} Pb was leached after the 28-day operation. Increasing the ratio from 5% to 7% only slightly reduced the concentration of Pb in the leachate. These findings, together with the BCR results, corroborate the effectiveness of M-AGS as a material capable of immobilizing Pb in contaminated soils, thus showing promise in minimizing the toxicity of the active fractions. As elaborated above, the enhancement of Pb stabilization with the aid of M-AGS should be conducive to firm complexation between the heavy metal and the abundant functional groups in the material, the formation of insoluble Pb precipitates, and more importantly, the possible incorporation of Pb in the inner structure of the Fe matrix.

4. Conclusion

We demonstrated that the utilization of magnetite helped to incorporate greater amounts of Fe oxides into the inner structure of AGSs, and the resulting M-AGS effectively promoted methane production. More importantly, the M-AGS achieved an enhanced adsorption capacity for Pb, which was superior to its AGS counterparts without the involvement of Fe oxides and those with ferrihydrite and hematite. Particularly noted is that the M-AGS significantly promoted the proportion of structural Pb that is difficult to extract by weak acids. The mechanistic studies have suggested that the formation of Pb-containing insoluble precipitates and the binding of Pb to the Fe oxide lattices accounts for this stabilization effect. These results have significant environmental implications, including i) the practical application of conductive magnetite to stimulate the growth of AGS that ultimately promotes methane generation from wastewater treatment and ii) the recycling of magnetic AGS as a promising adsorbent with several advantages, such as enhancement of adsorption capacity, promotion of heavy metal stabilization, and the feasibility of magnetic separation of adsorbed heavy metals from aqueous and soil media.

Declaration of Competing Interest

The authors declare that they have no known competing financial interests or personal relationships that could have appeared to influence the work reported in this paper.

Data availability

Data will be made available on request.

Acknowledgments

We gratefully acknowledge financial support from the National Key Research and Development Program of China (no. 2020YFC1808502); the National Natural Science Foundation of China (no. U21A2034); the Special Support Plan for Innovation Teams of Guangdong Province, China (no. 2019BT02L218); the Special Support Plan for Young Top-notch Talents of Guangdong Province, China (no. 2019TQ05L179); the Science and Technology Planning Project of Guangdong Province, China (no. 2019A050510009); and the Natural Science Foundation of Guangdong Province, China (no. 2021B1515120077).

Supplementary materials

Supplementary material associated with this article can be found, in the online version, at doi:10.1016/j.watres.2023.120022.

References

Ajao, V., Nam, K., Chatzopoulos, P., Spruijt, E., Bruning, H., Rijnaarts, H., Temmink, H., 2020. Regeneration and reuse of microbial extracellular polymers immobilised on a bed column for heavy metal recovery. Water Res. 171, 115472.

Al-Khateeb, L.A., Hakami, W., Abdel Salam, M., Sanari, J.A., El-Shaheny, R., El-Maghrabey, M., 2022. Solid phase-fabrication of magnetically separable Fe_3O_4@graphene nanoplatelets nanocomposite for efficient removal of NSAIDs from wastewater. Perception of adsorption kinetics, thermodynamics, and extra-thermodynamics. Anal. Chim. Acta 1223, 340158.

Baek, G., Jung, H., Kim, J., Lee, C., 2017. A long-term study on the effect of magnetite supplementation in continuous anaerobic digestion of dairy effluent-magnetic separation and recycling of magnetite. Bioresour. Technol. 241, 830–840.

Barakat, M.A., 2011. New trends in removing heavy metals from industrial wastewater. Arab. J. Chem. 4 (4), 361–377.

Basu, M., Guha, A.K., Ray, L., 2017. Adsorption of lead on cucumber peel. J. Clean. Prod. 151, 603–615.

Bhateria, R., Singh, R., 2019. A review on nanotechnological application of magnetic iron oxides for heavy metal removal. J. Water Process Eng. 31, 100845.

Bilal, M., Ihsanullah, I., Younas, M., UlHassan Shah, M., 2021. Recent advances in applications of low-cost adsorbents for the removal of heavy metals from water: a critical review. Sep. Purif. Technol. 278, 119510.

Caporale, A.G., Violante, A., 2015. Chemical processes affecting the mobility of heavy metals and metalloids in soil environments. Curr. Pollut. Rep. 2 (1), 15–27.

Chen, H., Tan, W., Lv, W., Xiong, J., Wang, X., Yin, H., Fang, L., 2020. Molecular mechanisms of lead binding to ferrihydrite-bacteria composites: ITC, XAFS, and mu-XRF Investigations. Environ. Sci. Technol. 54 (7), 4016–4025.

China, General administration of quality supervision inspection and quarantine of the people's republic of China, 2017. Standard For Groundwater Quality (GB/T 14848-2017). Standards press of China, Beijing.

Chisholm-Brause, C.J., Hayes, K.F., Roe, A.L., Brown Jr, G.E., Parks, G.A., Leckie, J.O., 1990. Spectroscopic investigation of Pb (II) complexes at the γ-Al_2O_3/water interface. Geochim. Cosmochim. Ac. 54 (7), 1897–1909.

Cruz Viggi, C., Rossetti, S., Fazi, S., Paiano, P., Majone, M., Aulenta, F., 2014. Magnetite particles triggering a faster and more robust syntrophic pathway of methanogenic propionate degradation. Environ. Sci. Technol. 48 (13), 7536–7543.

Cui, P., Wang, S., Su, H., 2022. Enhanced biohydrogen production of anaerobic fermentation by the Fe_3O_4 modified mycelial pellets-based anaerobic granular sludge. Bioresour. Technol. 366, 128144.

Daou, T.J., Pourroy, G., Begin Colin, S., Greneche, J.M., Ulhaq Bouillet, C., Legare, P., Bernhardt, P., Leuvrey, C., Rogez, G., 2006. Hydrothermal synthesis of monodisperse magnetite nanoparticles. Chem. Mater. 18, 4399–4404.

Dave, P.N., Chopda, L.V., 2014. Application of iron oxide nanomaterials for the removal of heavy metals. J. Nanotechnol. 2014, 1–14.

Esrafili, L., Firuzabadi, F.D., Morsali, A., Hu, M.L., 2021. Reuse of predesigned dual-functional metal organic frameworks (DF-MOFs) after heavy metal removal. J. Hazard. Mater. 403, 123696.

Feng, J., Zhang, J., Song, W., Liu, J., Hu, Z., Bao, B., 2020. An environmental-friendly magnetic bio-adsorbent for high-efficiency Pb(II) removal: preparation, characterization and its adsorption performance. Ecotoxicol. Environ. Saf. 203, 111002.

Frierdich, A.J., Helgeson, M., Liu, C., Wang, C., Rosso, K.M., Scherer, M.M., 2015. Iron atom exchange between hematite and aqueous Fe(II). Environ. Sci. Technol. 49 (14), 8479–8486.

Gahlot, P., Ahmed, B., Tiwari, S.B., Aryal, N., Khursheed, A., Kazmi, A.A., Tyagi, V.K., 2020. Conductive material engineered direct interspecies electron transfer (DIET) in anaerobic digestion: mechanism and application. Environ. Technol. Innovat. 20, 101056.

Hawari, A.H., Mulligan, C.N., 2006. Biosorption of lead(II), cadmium(II), copper(II) and nickel(II) by anaerobic granular biomass. Bioresour. Technol. 97 (4), 692–700.

Ji, J., Chen, G., Zhao, J., 2019. Preparation and characterization of amino/thiol bifunctionalized magnetic nanoadsorbent and its application in rapid removal of Pb (II) from aqueous system. J. Hazard. Mater. 368, 255–263.

Kang, H.J., Lee, S.H., Lim, T.G., Park, J.H., Kim, B., Buffiere, P., Park, H.D., 2021. Recent advances in methanogenesis through direct interspecies electron transfer via conductive materials: a molecular microbiological perspective. Bioresour. Technol. 322, 124587.

Karami, H., 2013. Heavy metal removal from water by magnetite nanorods. Chem. Eng. J. (Lausanne) 219, 209–216.

Kaur, N., Gräfe, M., Singh, B., Kennedy, B., 2009. Simultaneous incorporation of Cr, Zn, Cd, and Pb in the goethite structure. Clays Clay Miner. 57 (2), 234–250.

Kim, J., Choi, H., Lee, C., 2022. Formation and characterization of conductive magnetite-embedded granules in upflow anaerobic sludge blanket reactor treating dairy wastewater. Bioresour. Technol. 345, 126492.

Li, F., Yang, B., Yang, F., Wu, J., Chen, J., Song, S., Jia, J., 2023. Stabilization mechanism of Pb with an amino- and mercapto-polymer to assist phytoremediation. J. Hazard. Mater. 442, 130139.

Li, N., Quan, X., Zhuo, M., Zhang, X., Quan, Y., Liang, P., 2022a. Enhancing methanogenesis of anaerobic granular sludge by incorporating Fe/Fe oxides nanoparticles aided with biofilm disassembly agents and mediating redox activity of extracellular polymer substances. Water Res. 216, 118293.

Li, Y., Bian, Y., Qin, H., Zhang, Y., Bian, Z., 2017. Photocatalytic reduction behavior of hexavalent chromium on hydroxyl modified titanium dioxide. Appl. Catal., B 206, 293–299.

Li, Y., Tan, M., Liu, G., Si, D., Chen, N., Zhou, D., 2022b. Thiol-functionalized metal–organic frameworks embedded with chelator-modified magnetite for high-efficiency and recyclable mercury removal in aqueous solutions. J. Mater. Chem. A 10 (12), 6724–6730.

Li, Z., Kong, Y., Ge, Y., 2015. Synthesis of porous lignin xanthate resin for Pb^{2+} removal from aqueous solution. Chem. Eng. J. (Lausanne) 270, 229–234.

Ling, L.L., Liu, W.J., Zhang, S., Jiang, H., 2017. Magnesium oxide embedded nitrogen self-doped biochar composites: fast and high-efficiency adsorption of heavy metals in an aqueous solution. Environ. Sci. Technol. 51 (17), 10081–10089.

Liu, J., Huang, Z., Chen, Z., Sun, J., Gao, Y., Wu, E., 2020. Resource utilization of swine sludge to prepare modified biochar adsorbent for the efficient removal of Pb(II) from water. J. Clean. Prod. 257, 120322.

Lu, Y., Hu, S., Liang, Z., Zhu, M., Wang, Z., Wang, X., Liang, Y., Dang, Z., Shi, Z., 2020. Incorporation of Pb(II) into hematite during ferrihydrite transformation. Environ. Sci.: Nano 7 (3), 829–841.

Luo, T., Xu, Q., Wei, W., Sun, J., Dai, X., Ni, B.J., 2022. Performance and mechanism of Fe_3O_4 improving biotransformation of waste activated sludge into liquid high-value products. Environ. Sci. Technol. 56 (6), 3658–3668.

Ma, K., Wang, W., Liu, Y., Bao, L., Cui, Y., Kang, W., Wu, Q., Xin, X., 2021. Insight into the performance and microbial community profiles of magnetite-amended anaerobic digestion: varying promotion effects at increased loads. Bioresour. Technol. 329, 124928.

Ma, Y., Cheng, L., Zhang, D., Zhang, F., Zhou, S., Ma, Y., Guo, J., Zhang, Y., Xing, B., 2022. Stabilization of Pb, Cd, and Zn in soil by modified-zeolite: mechanisms and evaluation of effectiveness. Sci. Total Environ. 814, 152746.

Mahdavian, A.R., Mirrahimi, M.A.-S., 2010. Efficient separation of heavy metal cations by anchoring polyacrylic acid on superparamagnetic magnetite nanoparticles through surface modification. Chem. Eng. J. (Lausanne) 159 (1–3), 264–271.

Namdeo, M., 2018. Magnetite nanoparticles as effective adsorbent for water purification-A review. Adv. Recycl. Waste Manag. 02 (03), 1000135.

Nancharaiah, Y.V., Kiran Kumar Reddy, G., 2018. Aerobic granular sludge technology: mechanisms of granulation and biotechnological applications. Bioresour. Technol. 247, 1128–1143.

Naushad, M., Ahamad, T., Al-Sheetan, K.M., 2021. Development of a polymeric nanocomposite as a high performance adsorbent for Pb(II) removal from water medium: equilibrium, kinetic and antimicrobial activity. J. Hazard. Mater. 407, 124816.

Niu, Z., Zhang, Z., Liu, S., Miyoshi, T., Matsuyama, H., Ni, J., 2016. Discrepant membrane fouling of partial nitrification and anammox membrane bioreactor operated at the same nitrogen loading rate. Bioresour. Technol. 214, 729–736.

Pagliaccia, B., Carretti, E., Severi, M., Berti, D., Lubello, C., Lotti, T., 2022. Heavy metal biosorption by Extracellular Polymeric Substances (EPS) recovered from anammox granular sludge. J. Hazard. Mater. 424 (Pt C), 126661.

Qin, G., Niu, Z., Yu, J., Li, Z., Ma, J., Xiang, P., 2021. Soil heavy metal pollution and food safety in China: effects, sources and removing technology. Chemosphere 267, 129205.

Qu, C., Yang, S., Mortimer, M., Zhang, M., Chen, J., Wu, Y., Chen, W., Cai, P., Huang, Q., 2022. Functional group diversity for the adsorption of lead (Pb) to bacterial cells and extracellular polymeric substances. Environ. Pollut. 295, 118651.

Rauret, G., Lopez-Sanchez, J.F., Sahuquillo, A., Rubio, R., Davidson, C., Ure, A., Quevauviller, P., 1999. Improvement of the BCR three step sequential extraction procedure prior to the certification of new sediment and soil reference materials. J. Environ. Monit. 1 (1), 57–61.

Ravel, B., Newville, M., 2005. Athena, artemis, hephaestus: data analysis for X-ray absorption spectroscopy using IFEFFIT. J. Synchrotron Radiat. 12 (4), 537–541.

Ren, X., Chen, Y., Guo, L., She, Z., Gao, M., Zhao, Y., Shao, M., 2018. The influence of Fe ($^{2+}$), Fe($^{3+}$) and magnet powder (Fe_3O_4) on aerobic granulation and their mechanisms. Ecotoxicol. Environ. Saf. 164, 1–11.

Salam, A., Shaheen, S.M., Bashir, S., Khan, I., Wang, J., Rinklebe, J., Rehman, F.U., Hu, H., 2019. Rice straw and rapeseed residue-derived biochars affect the geochemical fractions and phytoavailability of Cu and Pb to maize in a contaminated soil under different moisture content. J. Environ. Manag. 237, 5–14.

Schwertmann, U., Taylor, R.M., 1989. Iron oxides. Min. Soil Environ. 1, 379–438.

Sharma, N.C., Gardea-Torresdey, J.L., Parsons, J., Sahi, S.V., 2004. Chemical speciation and cellular deposition of lead in *Sesbania drummondii*. Environ. Toxicol. Chem. 23 (9), 2068–2073.

Shi, J., Li, H., Lu, H., Zhao, X., 2015. Use of carboxyl functional magnetite nanoparticles as potential sorbents for the removal of heavy metal ions from aqueous solution. J. Chem. Eng. Data 60 (7), 2035–2041.

Si, S., Kotal, A., Mandal, T.K., Giri, S., Nakamura, H., Kohara, T., 2004. Size-controlled synthesis of magnetite nanoparticles in the presence of polyelectrolytes. Chem. Mater. 16, 3489–3496.

Sudmalis, D., Mubita, T.M., Gagliano, M.C., Dinis, E., Zeeman, G., Rijnaarts, H.H.M., Temmink, H., 2020. Cation exchange membrane behaviour of extracellular polymeric substances (EPS) in salt adapted granular sludge. Water Res. 178, 115855.

Tang, Y., Li, Y., Zhang, M., Xiong, P., Liu, L., Bao, Y., Zhao, Z., 2021. Link between characteristics of Fe(III) oxides and critical role in enhancing anaerobic methanogenic degradation of complex organic compounds. Environ. Res. 194, 110498.

Wang, C., Wang, C., Liu, J., Han, Z., Xu, Q., Xu, X., Zhu, L., 2020. Role of magnetite in methanogenic degradation of different substances. Bioresour. Technol. 314, 123720.

Wang, L., Wan, C., Lee, D.J., Liu, X., Zhang, Y., Chen, X.F., Tay, J.H., 2014. Biosorption of antimony(V) onto Fe(III)-treated aerobic granules. Bioresour. Technol. 158, 351–354.

Wang, L., Liu, X., Lee, D.J., Tay, J.H., Zhang, Y., Wan, C.L., Chen, X.F., 2018a. Recent advances on biosorption by aerobic granular sludge. J. Hazard. Mater. 357, 253–270.

Wang, M., Zhao, Z., Zhang, Y., 2021. Magnetite-contained biochar derived from fenton sludge modulated electron transfer of microorganisms in anaerobic digestion. J. Hazard. Mater. 403, 123972.

Wang, T., Zhang, D., Dai, L., Dong, B., Dai, X., 2018b. Magnetite triggering enhanced direct interspecies electron transfer: a scavenger for the blockage of electron transfer in anaerobic digestion of high-solids sewage sludge. Environ. Sci. Technol. 52 (12), 7160–7169.

Wang, Z.G., Lv, N., Bi, W.Z., Zhang, J.L., Ni, J.Z., 2015. Development of the affinity materials for phosphorylated proteins/peptides enrichment in phosphoproteomics analysis. ACS Appl. Mater. Interfaces 7 (16), 8377–8392.

Wei, X., Viadero Jr., R.C., Bhojappa, S, 2008. Phosphorus removal by acid mine drainage sludge from secondary effluents of municipal wastewater treatment plants. Water Res. 42 (13), 3275–3284.

Xu, Y., Boonfueng, T., Axe, L., Maeng, S., Tyson, T., 2006. Surface complexation of Pb (II) on amorphous iron oxide and manganese oxide: spectroscopic and time studies. J. Colloid Interface Sci. 299 (1), 28–40.

Yang, X., Wan, Y., Zheng, Y., He, F., Yu, Z., Huang, J., Wang, H., Ok, Y.S., Jiang, Y., Gao, B., 2019. Surface functional groups of carbon-based adsorbents and their roles in the removal of heavy metals from aqueous solutions: a critical review. Chem. Eng. J. 366, 608–621.

Yang, X., Zhang, X., Ma, Y., Huang, Y., Wang, Y., Chen, Y., 2009. Superparamagnetic graphene oxide–Fe_3O_4 nanoparticles hybrid for controlled targeted drug carriers. J. Mate. Chem. 19 (18), 2710–2714.

Ye, J., Hu, A., Ren, G., Chen, M., Tang, J., Zhang, P., Zhou, S., He, Z., 2018. Enhancing sludge methanogenesis with improved redox activity of extracellular polymeric substances by hematite in red mud. Water Res. 134, 54–62.

Zhang, M., Wang, Y., 2020. Effects of Fe-Mn-modified biochar addition on anaerobic digestion of sewage sludge: biomethane production, heavy metal speciation and performance stability. Bioresour. Technol. 313, 123695.

Zhang, T., Zhang, P., Hu, Z., Qi, Q., He, Y., Zhang, J., 2022. New insight on Fe-bioavailability: bio-uptake, utilization and induce in optimizing methane production in anaerobic digestion. Chem. Eng. J. 441, 136099.

Zheltova, V., Vlasova, A., Bobrysheva, N., Abdullin, I., Semenov, V., Osmolowsky, M., Voznesenskiy, M., Osmolovskaya, O., 2020. Fe3O4@HAp core–shell nanoparticles as MRI contrast agent: synthesis, characterization and theoretical and experimental study of shell impact on magnetic properties. Appl. Surf. Sci. 531, 147352.